THE EFFECTS OF CRACKING ON THE SURFACE POTENTIAL OF ICY GRAINS IN SATURN'S E-RING: LABORATORY STUDIES

Caixia Bu, David A. Bahr, Catherine A. Dukes, and Raúl A. Baragiola[1]
Laboratory for Astrophysics and Surface Physics, Materials Science and Engineering, University of Virginia, Charlottesville, VA 22904, USA; cb8nw@virginia.edu

ABSTRACT

Within Saturn's E-ring, dust grains are coated by water vapor co-released with ice grains from the geyser-like eruptions of Enceladus. These ice-coated grains have intrinsic surface potential and interact synergistically with the ions and electrons of Saturn's magnetospheric plasmas. We perform laboratory experiments to investigate the effects of water-ice growth on the surface potential, using amorphous solid water (ASW) films. We estimate the growth of the surface potential to be ~ -2.5 mV (Earth) yr^{-1} and -112 mV yr^{-1} for E-ring grains at $\sim 4.5 R_s$ and $3.95 R_s$ outside Enceladus's plume, respectively. In addition, our measurements show that the linear relationship between the surface potential and the film thickness, as described in previous studies, has an upper limit, where the film spontaneously cracks above a porosity-dependent critical thickness. Heating of the cracked films with (and without) deposited charge shows that significant positive (and negative) surface potentials are retained at temperatures above 110 K, contrary to the minimal values (roughly zero) for thin, transparent ASW films. The significant surface potentials observed on micron-scale cracked ice films after thermal cycling, $-(5-20)$ V, are consistent with *Cassini* measurements, which indicate a negative charge of up to -5 V for E-ring dust particles at $\sim 5 R_s$. Therefore, the native grain surface potential resulting from water-vapor coating must be included in modeling studies of interactions between E-ring icy surfaces and Saturn's magnetospheric plasma.

Key words: methods: laboratory: molecular – planets and satellites: fundamental parameters – planets and satellites: rings – planets and satellites: surfaces – plasmas

1. INTRODUCTION

Water ice is a principal constituent of many satellites, rings, and dust grains in the solar system (Schmitt et al. 1998; Baragiola 2003a). Measurements using *Cassini*'s Visual and Infrared Mapping Spectrometer instrument reveal that the surface of Enceladus, one of Saturn's satellites orbiting at a distance of $\sim 4 R_s$ (R_s is Saturn's equatorial radius, $R_s \approx 60,300$ km), is composed almost entirely of water ice (Brown et al. 2006). Similarly, Saturn's E-ring, extending from $\sim 3 R_s$ to at least $8 R_s$, is found to consist of grains (0.3–3 μm) (Kempf et al. 2008) of predominantly water ice with minor but significant contributions from other ices—carbon dioxide, ammonia, molecular nitrogen—as well as silicates and organics (Hillier et al. 2007; Postberg et al. 2008; Hsu et al. 2015). The source for the E-ring grains, initially expected to originate from meteoritic impact ejecta from Saturn's moons, has been re-evaluated with the discovery of cryovolcanic plumes of Enceladus, one of the most remarkable findings of the *Cassini* spacecraft's mission to Saturn (Spencer et al. 2006). These plumes, consisting of gases and ice grains, are ejected from large fractures (also called "tiger strips") near the south polar region of Enceladus. The gaseous constituents of the plumes are dominated by water vapor ($\sim 90\%$), which escapes Enceladus's gravitational pull to fill the magnetosphere of Saturn (Waite et al. 2006). This ejected vapor deposits a fresh layer of ice with each eruption back onto the surface of Enceladus, atop the surfaces of nearby planetary bodies, and onto the dust/ice grains preexisting in the E-ring. Ice grains, emitted in conjunction with the vapor, are broadly classified into two types: slow, large, salt-rich grains that tend to fall back onto Enceladus's surface, and fast, salt-poor grains that escape

the satellite, supplying ice grains of the E-ring (Postberg et al. 2011).

Both Enceladus and the E-ring are located within Saturn's plasma environment, which consists mainly of electrons and water-group ions (H_2O^+, OH^+, O^+, and H_3O^+) and is dominated by the cold components of the energy spectrum ($T_e \approx 0.5-8$ eV, $T_i < 100$ eV; Wahlund et al. 2009). Thus, charging of the icy surfaces is expected. The response of charged grains to electromagnetic forces will result in different dynamics from the uncharged ones, which may explain rather complex phenomena, such as the narrow mass distribution of the E-ring (Showalter et al. 1991) and/or the recently discovered Saturnian dust streams (Kempf et al. 2005). A large number of models for the charging of E-ring grains resulting from ambient radiation such as plasma and solar UV photons have been presented; however, the published models predict electrostatic potentials of the grains varying by an order of magnitude (Morfill et al. 1993; Jurac et al. 1995; Kempf et al. 2006; Misra et al. 2012). With such a spread of values, it remains difficult to model the charge behavior of grains immersed in a planetary plasma environment.

Amorphous solid water (ASW) films grown in the laboratory by vapor condensation on cold substrates (below ~ 130 K; Baragiola 2003b, p. 359) serve as analogs for water-ice grains existing within Saturn's rings, which have temperatures of 70–110 K (without solar radiation) based on *Cassini*'s Composition Infrared Spectrometer (CIRS) data (Flasar et al. 2005). To simulate the water-vapor coating of the grains, we deposited ASW films with thicknesses to a few microns, within the range of ring particle sizes, and quantify the surface potential of the films during vapor deposition. Charging of E-ring grains by plasma ions was simulated by irradiation of ASW films with low-energy ions. A crucial characteristic of laboratory-prepared ASW films is the microporosity, defined as

---

[1] Deceased.

$\phi = 1 - \rho/\rho_c$, where ρ is the density of the ASW film and $\rho_c = 0.94$ g cm^{-3} is the density of the compact ice (Narten et al. 1976), which strongly depends on the deposition temperature (Mayer & Pletzer 1986), vapor deposition angle of incidence (Stevenson et al. 1999), and subsequent processing such as thermal annealing (Raut et al. 2007) or ion irradiation (Raut et al. 2008). Thus, to examine the role of microporosity on the spontaneous and ion-induced surface potential (Bu et al. 2015; Bu & Baragiola 2015), we vary the deposition temperature (T_g) and incidence angle of the vapor beam (θ). Temperature variation is expected between solar lit and unlit E-ring grains ($\sim$30 K hotter for rings lit by solar radiation based on *Pioneer* [Froidevaux & Ingersoll 1980] and *Voyager* [Hanel et al. 1981, 1982] data), optically thick and thin portions of the rings ($\sim$20–40 K cooler for the thick regions based on CIRS data; Flasar et al. 2005), and seasonal variation ($\sim$15 K based on CIRS data; Flasar et al. 2005). Thus, we also observe the evolution of the ASW surface potentials as a function of temperature.

2. EXPERIMENTAL DETAILS

Simulations of E-ring water-ice grain growth were conducted in an ultrahigh vacuum system with a base pressure of $\sim$2 × 10^{-10} Torr, described previously elsewhere (Bu et al. 2015; Bu & Baragiola 2015). ASW films were deposited by directing a collimated water vapor beam (Sack & Baragiola 1993) onto a gold-coated, liquid-helium-cooled quartz crystal microbalance (QCM, the substrate; Allodi et al. 2013) mounted on a copper target. The areal mass of each film was determined by changes in the frequency of the QCM resulting from deposition of condensed gases, which was subsequently converted into column density (in units of monolayers, ML, defined as 1 ML = 10^{15} molecules cm^{-2}) by dividing by the molecular mass; error for this method of extrapolating the column density is ±0.08 ML. The temperature of the condensed water ice was measured on the substrate using a silicon diode temperature sensor (Scientific Instruments, Si-410C) inserted in the target and regulated with a temperature controller (Lakeshore 330). The system was equipped with a UV–visible interferometer (FilmTek 2000) to measure the film thickness (Raut et al. 2008). The film density ρ, and therefore the microporosity ϕ, was calculated from the ratio of the film areal mass to the thickness. Surface potentials of the films were measured using a Kelvin probe (KP Technology Ltd., model UHV KP 4.5). The Kelvin probe is a noncontact device with a vibrating tip, which measures the contact potential difference (CPD) between the tip and the film; surface potentials of the ASW films are derived from the CPD measurements. The CPD measurements have a resolution better than 0.05 V, and the derived surface potentials have relative errors less than 2%. A long-distance microscope (Questar QM-100) was set at 45° relative to the sample normal to allow simultaneous observation of any changes in the film microstructures. The microscope was at a working distance of 23 cm, and a digital camera was used to take time-sequenced photographs with a spatial resolution of $\sim$3 μm.

During growth of a film, the substrate (QCM) was kept at a constant temperature (the deposition temperature, T_g); the vapor beam was at a constant angle relative to the QCM normal (the incidence angle, θ) and was controlled by adjusting a leak valve such that the frequency of the QCM decreased by a constant rate of 1.7 ± 0.2 Hz s^{-1} (equal to a deposition rate of

0.7 ± 0.1 ML s^{-1}). To investigate the thermal-induced effects, the ASW films were warmed using a resistive heater on the target with a temperature ramp rate of 4.8 K minute^{-1}, and surface potentials were measured as a function of temperature. To simulate positive charging of ice grains in the E-ring from interaction with (positive) plasma ions, the ASW films were charged by irradiating with 500 eV helium ions (He$^+$) prior to warming. The ions were produced by a low-energy ion gun (Nonsequitur Technologies, Model 1401) at normal incidence using a constant fluence of (0.9 ± 0.1) × 10^{12} He$^+$ cm^{-2}. Beam flux was measured with a Faraday cup and kept constant at (0.33 ± 0.04) × 10^{10} He$^+$ cm^{-2} s^{-1}. Ions in Saturn's inner plasma are dominated by water-group ions at energies below $\sim$100 eV (Wahlund et al. 2009). Here we use He$^+$, which is chemically inert, for laboratory simulations to avoid the complexity of potential chemical reactions; we set the ion energy at 500 eV rather than 100 eV or below, so that we could observe the beam location on the sample while minimizing the sample damage. The penetration of He$^+$ at 500 eV in water ice is less than 0.02 μm, based on Transport of Ions in Matter simulations (Ziegler & Biersack 2013), much smaller than the thickness of the films. Thus, the positive charges reside within a very thin surface layer atop the ASW film (Bu & Baragiola 2015), a reasonable simulation for the charged icy grains of the E-ring. The transport of *positive* charge in thin *amorphous* water-ice films has been discussed in detail by Fisher & Devlin (1995) and recently by Bu & Baragiola (2015). The mechanism is different than for *crystalline* and *polycrystalline* ice films ($T \geqslant 120$ K), where charge transport involves the successive passage of proton and orientational defects, resulting in enhanced proton mobility on the surface of ice films (Park et al. 2004; Devlin 2011). For ASW the ion transport process is less clear, since the mobility of possible defects is extremely limited at temperatures below $\sim$100 K (Fisher & Devlin 1995). In this regime incompletely coordinated molecules, negligible in crystalline ice but abundant in ASW (Buch & Devlin 1991; Raut et al. 2007), play a primary role and result in long-range charge migration along the walls of the pores (Bu & Baragiola 2015).

3. RESULTS AND DISCUSSION

3.1. Spontaneous Negative Surface Potentials for ASW Ice

The appearance of negative surface potentials during growth of water-ice films at low temperatures ($<$100 K) has been known for decades (Kutzner 1972; Tsekouras et al. 1998; Bu et al. 2015). The native surface potential for water ice can vary greatly in magnitude, but, for thin films ($\sim$1100 ML, $<$0.5 μm) as reported by Bu et al. (2015), these values are between $\sim$−5 and −22 V. Also, for thicknesses less than 0.5 μm, the magnitude of the negative surface potential ($|V_s|$) increases linearly with thickness with a slope that depends on film porosity (Bu et al. 2015). The *negative* surface potentials of the water-ice films are attributed to an alignment of the incompletely coordinated molecules (Buch & Devlin 1991) on the walls of the pores, and values of $|V_s|$ correlate well with the abundance of these molecules (Bu et al. 2015). If the linear relationship between the $|V_s|$ and thickness continues to hold for films up to a few microns, the depth of potential E-ring grain ice coatings, it should be possible to extrapolate the surface potentials for all ice-coated planetary surfaces, given the thickness of the ice. Thus, we investigate surface potential
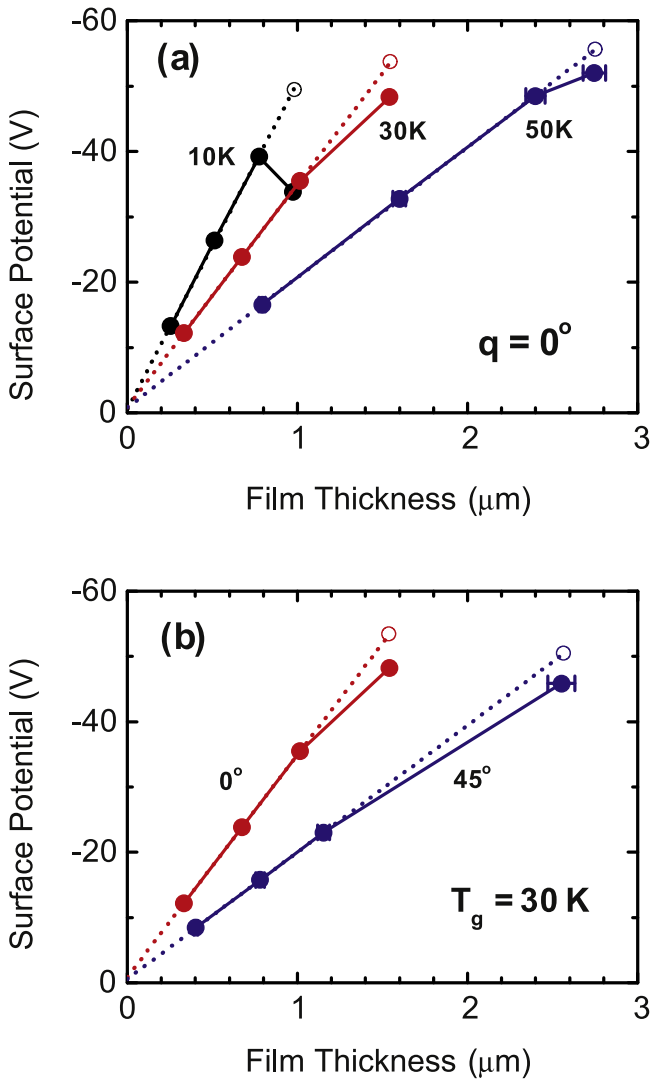
Figure 2. Optical microscope images of transparent and cracked ASW ice films. The field of view is 1.4 mm in diameter, and images are at the same position on the sample substrate (QCM). Left: a thin, transparent film below the critical thickness (L_c); right: thick, cracked films at the critical thickness L_c for varied porosities controlled by (a) deposition temperature and (b) incidence angle.

Figure 1. Evolution of intrinsic negative surface potentials (V_s) during growth of ASW films (filled circles connected with solid lines; the x- and y-error bars are smaller than the size of the circles if not shown in the graph). The magnitude of the V_s ($|V_s|$) initially increases linearly with film thickness, until the film thickness reaches a critical thickness (the filled circle on each solid line with the greatest thickness), at which the $|V_s|$ abruptly decreases if compared to the value extrapolated from the linear fit (open circles). (a) ASW films were deposited at 10, 30, and 50 K at normal incidence. The density of the films was 0.84 g cm^{-3}. (b) ASW films were deposited at 30 K at incidence angles of 0° and 45°. The film densities were 0.84 and 0.69 g cm^{-3}; thus, the porosities were 0.11 and 0.27, respectively.

evolution as a function of thickness for films up to several microns.

ASW films were deposited at different temperatures (T_g = 10, 30, and 50 K) at normal incidence ($\theta = 0°$), with a constant deposition rate (0.7 ± 0.1) ML s^{-1}, that is, the frequency of the QCM decreases at a constant rate of ~1.7 Hz s^{-1}. Surface potentials (V_s) of the films were measured as a function of film thickness. Results are shown in Figure 1(a). For films <0.7 μm, V_s versus film thickness is linear (Figure 1(a), dashed lines) at a rate that decreases with increasing T_g, consistent with results using thin films (Bu et al. 2015). However, the linear relationship has an upper limit: the measured magnitude of the film voltages ($|V_s|$) shows an abrupt decrease at a critical thickness (Figure 1(a), filled circles with
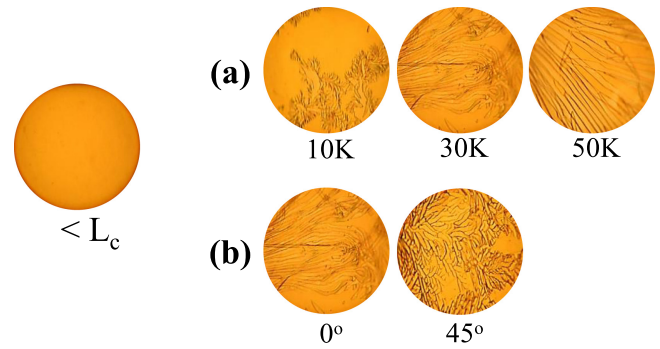
greatest thicknesses), compared to the corresponding extrapolated value using the straight-line fit (Figure 1(a), open circles). Simultaneously, at the critical thickness, we noticed an abrupt, significant change in the frequency of the QCM. The growth of the ASW film was terminated when the sharp change in the QCM frequency was observed, and the critical thickness was determined using the frequency of the QCM and the density of the film immediately before the onset of the sharp change.

To understand the cause of the sudden, sharp decrease in $|V_s|$ with film thickness, we note that the critical thickness increases with growth temperature T_g (Figure 1(a)), which suggests that changes in porosity may impact the value of the critical thickness. Indeed, Figure 1(a) indicates that the critical thickness increases as the porosity decreases, since porosity (more precisely, the abundance of the incompletely coordinated molecules) is inversely correlated with T_g (Buch & Devlin 1991; Raut et al. 2007).

We tested the possible effects of porosity by depositing ASW films with different incidence angles ($\theta = 0°$ and 45°) at 30 K, since porosity increases with vapor deposition angle (Stevenson et al. 1999), and measured the V_s as a function of film thickness; results are shown in Figure 1(b). Again, we find that above a critical thickness the linear relationship between the V_s and film thickness no longer holds. From Figure 1(a), we expected that the critical thickness would be larger in the case of $\theta = 0°$, where the porosity is smaller. However, surprisingly the critical thickness is larger in the case of $\theta = 45°$, where the porosity is greater.

In addition, interference patterns for measurements using the UV–visible interferometer disappeared on reaching the critical thickness, although thickness-independent ice densities were obtained from measurements at all thicknesses below the critical ones. The observed loss of the interference patterns suggests significant changes in morphology, leading us to examine the microstructure of the films. Laboratory-prepared porous thin ASW films are expected to be transparent, since the inferred dimensions of the pores (1–2 nm; Raut et al. 2007) are much smaller than the optical wavelength and the pores do not contribute appreciably to the scattering. Indeed, we observed transparent ASW films below the critical thickness (Figure 2, left panel). However, at the critical thickness, microscope images of the films (Figure 2, right panels (a) and (b)) show that the ASW films crack spontaneously. Thus, we attribute the
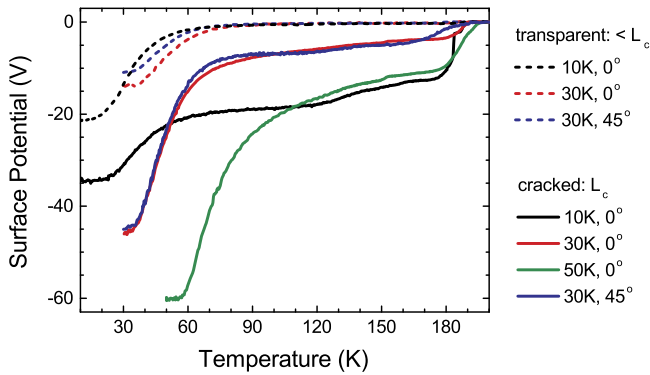
Figure 3. Thermal evolution of ASW film surface potentials. Films were warmed from deposition temperature T_g to 200 K at a rate of 4.8 K minute^{-1}. Cracked films (solid lines) were prepared at T_g = 10, 30, and 50 K at θ = 0° and at T_g = 30 K at θ = 45°, with the critical thickness (L_c, in units of μm) of (0.96 ± 0.03), (1.54 ± 0.03), (2.74 ± 0.07), and (2.54 ± 0.06), respectively. The 1100 ML thin, transparent films (dashed lines) (Bu et al. 2015) were prepared at T_g = 10 and 30 K at θ = 0°, and at T_g = 30 K at θ = 45°, with the thickness (in units of μm) of (0.39 ± 0.02), (0.39 ± 0.02), and (0.48 ± 0.02), respectively. (Adapted with permission from C. Bu et al., J. Chem. Phys. 142, 134702 (2015). Copyright 2015 AIP Publishing LLC.)

observed sudden decreases of the $|V_s|$ at the critical thicknesses (Figure 1) to the onset of the cracking, rather than porosity.

Figure 1 shows that the critical thickness increases with T_g and θ. The corresponding cracks in the films develop from small-scale, dense, ramified patterns to large, sparse, increasingly linear ones as the T_g increases (Figure 2(a)), and from long, line-like patterns toward small, block-like ones as the θ increases (Figure 2(b)). We study the spontaneous cracking of ASW films in detail in a companion publication and propose that the cracking of ASW films is caused by the intrinsic stresses resulting from the film porosities (C. Bu et al. 2016, in preparation). The component of the stresses contributing to the occurrence of the cracking is suggested to decrease with increasing T_g and θ, explaining the dependences of the critical thickness on the T_g and θ (Figure 1), and the developing trends of the cracks (Figures 2(a) and (b)) are correlated with the energy released during the cracking (Griffith 1921; C. Bu et al. 2016, in preparation). The deviation of $|V_s|$ at the critical thickness (that is, the vertical distance between the open and filled circles at the onset of the cracking in Figure 1) may be related to the released energy during cracking, an interesting topic for future study.

3.2. Effects of Thermal Processing on ASW Negative Surface Potential

Transparent ASW films less than 0.5 μm show that the magnitude of the inherent negative surface potential ($|V_s|$) decreases by 80% when the ice film is warmed to ⩾30 K above the deposition temperature T_g (Figure 3 dashed lines), and the $|V_s|$ cannot be recovered by re-cooling the films (Bu et al. 2015). This was attributed to the thermal-induced reorientation of the incompletely coordinated molecules on the pore walls (Buch & Devlin 1991; Bu et al. 2015). However, as shown in Section 3.1, ASW films crack spontaneously when the film thicknesses exceed the critical thicknesses, which may affect the thermal evolutions of the $|V_s|$.

To study the thermal-induced change in surface potential (V_s), we prepared ASW films at different temperatures (T_g = 10, 30, and 50 K) with θ = 0°, where growth was

terminated when the films cracked. We also prepared a cracked ASW film at T_g = 30 K at θ = 45°, to study the potential effects of porosity. After growth, the cracked films were heated from the T_g to 200 K at a rate of 4.8 K minute^{-1}, and V_s of the films was monitored as a function of temperature. Results are shown in Figure 3 (solid lines). Compared with results for the thin, transparent films (Bu et al. 2015), the cracked films retain significant surface potentials when warmed to temperatures much higher than 30 K above the T_g. For instance (Figure 3), the V_s of the cracked film deposited at 30 K is ~−6 V (~13% of the initial value of −46 V at 30 K) at 110 K, compared to ~0 V of the transparent film warmed at the same temperature. Evolutions of the V_s of the cracked films with different porosities (T_g = 30 K, θ = 0° and 45°) are similar, suggesting that the distinctive features of the V_s versus temperature curves of the cracked films result mainly from the cracks rather than the porosity. We note that ASW ice (at pressure <10^{-9} Torr) sublimates at ~180 K (Sack & Baragiola 1993), indicated by the sudden change of V_s to zero (Figure 3).

3.3. Effects of Deposited Surface Charge on ASW Surface Potential

Interactions of the plasma ions (made up of primarily positive water-group ions; Wahlund et al. 2009) with the icy grain surfaces within Saturn's plasma environment should result in positive surface potentials (V_+), since the ions both deposit positive charge and eject negative secondary electrons (Shi et al. 2010). We simulated this charging process by irradiating cracked ASW films (>1 μm) using 500 eV helium ions (He$^+$) and then measured the thermal-induced evolution of the V_+.

When ions deposit a positive charge Q on top of a very thin surface layer of an insulator (like ASW ice) on an electrically grounded metal substrate, a surface potential (V_+) is created, given by $V_+ = (Q/A) \times [d/(\varepsilon \varepsilon_o)]$, where A is the irradiated area, d the film thickness, ε the dielectric constant of the film, and ε_o = 8.854 × 10^{-14} C V^{-1} cm^{-1} the permittivity of vacuum. Similar to uncharged films, recent studies for charged transparent ASW films (<0.5 μm) show that the V_+ decreases sharply once the charged film is warmed, and the V_+ drops to ~0 V above a temperature 30 K higher than T_g (Figure 4, dashed lines; Bu & Baragiola 2015). The thermal-induced sharp decrease in the V_+ is attributed to charge migration along the walls of the pores, facilitated by the thermally induced reorientation of the incompletely coordinated molecules on the pore walls (Buch & Devlin 1991; Bu & Baragiola 2015). Because cracking destroys the pore network, this proposed discharging mechanism does not necessarily hold for films greater than the critical thickness (cracked films).

To better understand the effects of surface charge on icy grains, we utilized cracked ASW films (>1 μm) as E-ring grain analogs, prepared at different deposition temperatures (T_g = 10, 30, and 50 K) and incidence angles (θ = 0° and 45°) as described in Section 3.2. After growth, charge was deposited onto the surface of the cracked films at T_g, by irradiating to fluences of ~(0.9 ± 0.1) × 10^{12} He$^+$ cm^{-2} at normal incidence. The charged, cracked films were then warmed from the T_g to 200 K at a rate of 4.8 K minute^{-1}, and surface potentials of films (V_+) were measured as a function of temperature (Figure 4, solid lines). We observed sharp decreases in V_+ above T_g, similar to the transparent films (Bu & Baragiola 2015). However, the curves of V_+ versus temperature of the
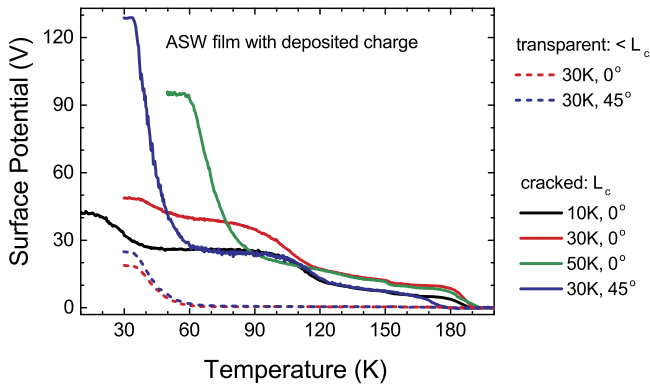
Figure 4. Thermal evolution of the surface potentials for charged films (V_+) during warming from the deposition temperature (T_g) to 200 K at a rate of 4.8 K minute^{-1}. Prior to warming, the films were irradiated at T_g with 500 eV He$^+$ to fluences of $(0.9 \pm 0.1) \times 10^{12}$ He$^+$ cm^{-2}. Cracked films (solid lines) were prepared at $T_g = 10, 30,$ and 50 K at $\theta = 0°$ and at $T_g = 30$ K at $\theta = 0°$, with the critical thickness (L_c, in units of μm) of 0.96 ± 0.03, 1.54 ± 0.03, 2.74 ± 0.07, and 2.54 ± 0.06, respectively. The 1100 ML thin, transparent films (dashed lines) (Bu & Baragiola 2015) were prepared at $T_g = 30$ K at $\theta = 0°$ and $\theta = 45°$, with the thickness (in units of μm) of 0.39 ± 0.02 and 0.48 ± 0.02, respectively. (Adapted with permission from C. Bu, and R. A. Baragiola, J. Chem. Phys. 143, 074702 (2015). Copyright 2015 AIP Publishing LLC.)

cracked films display several distinctive features: greater V_+, rather than ~0 V, is retained at heating temperatures greater than 30 K above the T_g, and two additional sharp decreases in V_+ at ~100 and ~180 K. For example, the cracked film deposited at $T_g = 30$ K at $\theta = 0°$ has a V_+ of ~22 V at 110 K (~45% the initial value of 49 V at 30 K), while thin, transparent (uncracked) ASW films have V_+ of ~0.8 V at 110 K (~4% of the initial value of 19 V at 30 K); the V_+ of the cracked film shows a second steep decrease from ~33 to 17 V at 95–120 K and a final steep change from ~10 to ~0 V at 175–190 K, while no corresponding decreases in V_+ were observed in the transparent film deposited at the same T_g and θ. The larger V_+ preserved in the cracked films suggests that a significant proportion of the deposited charges are trapped in the cracked films during warming, most likely at the crack-induced defects, rather than migrating to the substrate like in the transparent films. Above ~100 K, activated defects, bulk diffusion, and crystallization facilitate the migration of the trapped charges (Fisher & Devlin 1995; Devlin 2011), resulting in the sharp decrease of the V_+ at ~100 K. We attribute the sharp decrease of V_+ in the cracked films at ~180 K to the sublimation of the ice films (Sack & Baragiola 1993) and/or the increased rate for charge transport (Fisher & Devlin 1995) at such high temperature.

4. ASTROPHYSICAL IMPLICATIONS

Saturn's satellites and ring particles are exposed to the surrounding plasma environment, and nonconducting ice and ice-coated silicates or carbonaceous materials charge rapidly due to interactions with the electrons and ions. The charging of E-ring particles has been studied previously, with published charging models taking into account secondary electron emission (Jurac et al. 1995), sputtering of the icy surface (Jurac et al. 2001), size and shape of the grains (Kempf et al. 2006), and grain compositions (Misra et al. 2012). However, the distinct native electrical properties of water ice as shown in this work have not been discussed.

The discovery of plumes ejecting gaseous and solid water from the south polar region of Enceladus supports its special role in supplying water vapor—both neutral and ionized constituents—to the magnetosphere of Saturn, as well as ice grains directly into the E-ring (Spencer et al. 2006). Results from *Cassini*'s Ion Neutral Mass Spectrometer measurements find that the average abundance of neutral water molecules (H$_2$O) in the E-ring is ~1.9×10^3 H$_2$O cm^{-3} at distances far from Enceladus ($4.5R_s$; Perry et al. 2010), ~8.5×10^4 H$_2$O cm^{-3} near Enceladus but outside its plume ($3.95R_s$, north of the equatorial plane; Perry et al. 2010), and ~$(7.6–34) \times 10^7$ H$_2$O cm^{-3} within Enceladus's plume (Teolis et al. 2010).

Using laboratory data at 50 K—a reasonable temperature for Saturn's rings—we estimate the surface potential for E-ring grains in these three regions, using a unitary sticking probability for neutral water molecules on icy surfaces. Assuming a single spherical silicate grain (with a diameter of d_g) embedded in a neutral H$_2$O background (with a density of N_w), we use a simple model based on collisional kinetic theory (Sears 1952) to determine the rate ($R_{g\cdot w}$) at which H$_2$O molecules (diameter d_W) collide with the grain. Since $d_g \gg d_W$, the effective collision area is $S = (\pi d_g^2)/4$ with estimated relative velocity: $v_r = [(8k_BT)/(\pi M_w)]^{1/2}$ where k_B is the Boltzmann constant, given that the grain mass M_g is much larger than the water molecule mass M_w. Therefore, the number of H$_2$O collisions for one grain per unit time is $R_{g\cdot w} = S v_r N_w$. For a spherical model grain with surface area $A = \pi d_g^2$, we estimate the amount of H$_2$O required for 1 ML (1 ML = 10^{15} H$_2$O cm^{-2}) complete grain coverage $C_{Total} = A \times 10^{15}$ H$_2$O cm^{-2} ML^{-1}, and the coating time t per ML can be determined from $t_{ML} = C_{Total}/R_{g\cdot w}$. Thus, using a relative velocity for $T = 50$ K ($v_r = 242$ m s^{-1}), we estimate the rate of coverage for E-ring grains ($1/t_{ML}$) by H$_2$O ejected by Enceladus is ~1.2×10^{-8} ML s$^{-1} \approx 0.36$ ML (Earth) yr^{-1}, 16 ML yr^{-1}, and $(1.4–6.5) \times 10^4$ ML yr^{-1} at ~$4.5R_s$, ~$3.95R_s$ outside the plume, and ~$3.95R_s$ within the plume, respectively. At $T_g = 50$ K, the growth rate of the inherent negative surface potential is ~-7 mV ML^{-1} (Figure 1); thus, the development of the surface potential of icy grains in the three locations is ~-2.5 mV (Earth) yr^{-1}, -112 mV yr^{-1}, and $-(1.0–4.6) \times 10^2$ V yr^{-1}, respectively. Of course, the water-vapor coating for E-ring grains may be deposited at a faster or slower rate, depending on the distance of the grains from Enceladus, local temperature, sputtering, the eruptive activity of Enceladus, etc. However, over the astrophysical lifetime of the grains, it is likely that negative surface potentials with magnitudes of a few volts to several hundred volts can be built up. Indeed, measurements from *Cassini*'s Cosmic Dust Analyser, as well as the Radio and Plasma Wave Science instrument, indicate that the E-ring dust particles are negatively charged, up to -5 V at ~$5R_s$ (Wahlund et al. 2005; Kempf et al. 2006; Morooka et al. 2011).

While these negative surface potentials may be mitigated by irradiation with energetic magnetospheric particles with energies from a few tens to hundreds of keV, which deposit positive charge and eject multiple secondary electrons on impact (Shi et al. 2010), Saturn's plasma near Enceladus and the E-ring is dominated by cold electrons ($T_e < 8$ eV) and water-group ions (H$_2$O$^+$, OH$^+$, O$^+$, and H$_3$O$^+$) ($T_i < 100$ eV; Wahlund et al. 2009), with a small component (~3%) of cold N$^+$ (Young et al. 2005). Thus, the native negative surface potential for icy or ice-coated grains is sufficient to affect the

charge fluxes that reach the grain by reflecting (attracting) most of the electrons (positive ions) and must be considered when studying the charging of the icy surfaces resulting from plasma interaction and modeling the dynamics of the surrounding cold plasma.

Prior to this study on cracked ASW surface potentials, it could be argued that the negative surface potentials of ice-covered grains may be neglected in charging models, since the potentials drastically diminish or disappear with thermal cycling. Indeed, studies using transparent ASW films less than 0.5 μm suggest that an increase of $\sim$30 K in temperature, close to the thermal fluctuations in most icy satellites and moons (Froidevaux & Ingersoll 1980; Hanel et al. 1981, 1982; Flasar et al. 2005), is sufficient to remove $\sim$80% of the surface charge (Bu et al. 2015). Our studies here, however, show that ASW films crack when coating thickness exceeds the temperature-dependent critical thickness (Figure 1), typically a few microns. This implies that a significant proportion of the surface potential is retained when E-ring grain temperature cycles with solar radiation (Figure 3). For instance, an ice film deposited at $T_g = 50$ K at $\theta = 0°$ cracks if the film thickness exceeds $\sim$2.7 μm, within the E-ring grain size range, and a significant surface potential ($\sim$−18 V) of the cracked film is retained even at 110 K (Figure 3), which may deflect or even reflect (attract) the cold electrons (positive ions) reaching the surfaces. For cracked ice films with deposited surface charge ($\sim$1 $\times$ 10^{12} He$^+$ cm^{-2}) a similar trend is observed: for example, the surface potential of the cracked film deposited at $T_g = 50$ K is $\sim$20 V at 110 K (Figure 4), sufficient to affect the flux of the charged particles reaching the surfaces. We note that films were charged *after* growth in our laboratory simulations, while in astrophysical contexts plasma-ion charging and water-vapor coating are expected to be concurrent on the icy grains. Recent studies (Bu & Baragiola 2015) show that the inherent negative surface potential of the ice film develops similarly regardless of the substrate potential; that is, the development of the negative and positive components of the surface potential are independent and linearly additive for the determination of final surface charge. In addition, the negative and positive components of the surface potential respond independently to the thermal cycles.

Results here indicate that E-ring ice grains with H$_2$O coatings of a few microns likely still have surface potentials sufficient to affect their interaction with the surrounding plasma, even taking into account the thermal cycling. Thus, the effects of cracks on the surface potentials are of great importance and should be considered in simulations of the synergistic interaction between the icy surfaces and the surrounding low-energy plasma. We note that bombardment by more energetic particles (such as the high-energy tail of the plasma, solar wind, cosmic rays, etc.) on the ice surfaces can affect the overall surface potential of the grains by depositing charge (Shi et al. 2010), sputtering (Jurac et al. 2001), and destroying the underlying porosity (Raut et al. 2008); however, these energies do not dominate in the E-ring and are not included in our model.

5. SUMMARY AND CONCLUSION

Measurements of surface potential of ASW ice films show that a native negative surface voltage develops in the film with deposition; the magnitude of the negative surface voltage initially increases linearly with thickness, $\sim$−20 to −40 V for

1 μm films deposited at temperatures below 50 K, but decreases abruptly by 4–15 V when the thickness exceeds a critical value. This critical thickness is a function of the film porosity and is typically a few microns for deposition temperatures below 50 K. Microscopic images of the ice films indicate that films crack spontaneously at the critical thickness, causing the sharp decrease in the magnitude of the surface potential. The cracked films, with and without deposited charges, retain significant voltages as the temperature increases to as high as $\sim$110 K; in contrast, transparent films ($<$0.5 μm) retain minimal (almost zero) voltages with thermal cycling. We attribute the preserved voltage with increased temperature for cracked films to the crack-induced defects.

The unique electrical properties of ASW ice films have applications to the study of interactions between the planetary plasma and the embedded icy grains and/or planetary surfaces. We estimate the voltages resulting from the deposition of cryovolcanic water vapor onto the surface of Saturn's E-ring grains to vary from a few millivolts to hundreds of volts, depending on the location of the grain. Calculated grain potentials are sufficient to deflect and even reflect the dominant cold portions of Saturn's plasma. Thus, the effect of the surface potentials of the ice water must be considered when modeling charging processes in the Saturnian system.

REFERENCES

Allodi, M. A., Baragiola, R. A., Baratta, G. A., et al. 2013, SSRv, 180, 101
Baragiola, R. A. 2003a, P&SS, 51, 953
Baragiola, R. A. 2003b, in Water In Confining Geometries, ed. J. P. Devlin, & V. Buch (Berlin: Springer)
Brown, R. H., Clark, R. N., Buratti, B. J., et al. 2006, Sci, 311, 1425
Bu, C., & Baragiola, R. A. 2015, JChPh, 143, 074702
Bu, C., Shi, J., Raut, U., Mitchell, E. H., & Baragiola, R. A. 2015, JChPh, 142, 134702
Buch, V., & Devlin, J. P. 1991, JChPh, 94, 4091
Devlin, J. P. 2011, PCCP, 13, 19707
Fisher, M., & Devlin, J. P. 1995, JPhCh, 99, 11584
Flasar, F. M., Achterberg, R. K., Conrath, B. J., et al. 2005, Sci, 307, 1247
Froidevaux, L., & Ingersoll, A. P. 1980, JGR, 85, 5929
Griffith, A. A. 1921, RSPTA, 221, 163
Hanel, R., Conrath, B., Flasar, F. M., et al. 1981, Sci, 212, 192
Hanel, R., Conrath, B., Flasar, F. M., et al. 1982, Sci, 215, 544
Hillier, J. K., Green, S. F., McBride, N., et al. 2007, MNRAS, 377, 1588
Hsu, H.-W., Postberg, F., Sekine, Y., et al. 2015, Natur, 519, 207
Jurac, S., Baragiola, R. A., Johnson, R. E., & Sittler, E. C., Jr. 1995, JGR, 100, 14821
Jurac, S., Johnson, R. E., & Richardson, J. D. 2001, Icar, 149, 384
Kempf, S., Beckmann, U., Moragas-Klostermeyer, G., et al. 2008, Icar, 193, 420
Kempf, S., Beckmann, U., Srama, R., et al. 2006, P&SS, 54, 999
Kempf, S., Srama, R., Horanyi, M., et al. 2005, Natur, 433, 289
Kutzner, K. 1972, TSF, 14, 49
Mayer, E., & Pletzer, R. 1986, Natur, 319, 298
Misra, S., Mishra, S. K., & Sodha, M. S. 2012, MNRAS, 423, 176
Morfill, G. E., Havnes, O., & Goertz, C. K. 1993, JGR, 98, 11285
Morooka, M. W., Wahlund, J. E., Eriksson, A. I., et al. 2011, JGR, 116, A12221

Narten, A. H., Venkatesh, C. G., & Rice, S. A. 1976, JChPh, 64, 1106
Park, S. C., Jung, K. H., & Kang, H. 2004, JChPh, 121, 2765
Perry, M. E., Teolis, B., Smith, H. T., et al. 2010, JGR, 115, A10206
Postberg, F., Kempf, S., Hillier, J. K., et al. 2008, Icar, 193, 438
Postberg, F., Schmidt, J., Hillier, J. K., Kempf, S., & Srama, R. 2011, Natur, 474, 620
Raut, U., Fama, M., Loeffler, M. J., & Baragiola, R. A. 2008, ApJ, 687, 1070
Raut, U., Fama, M., Teolis, B. D., & Baragiola, R. A. 2007, JChPh, 127, 204713
Sack, N. J., & Baragiola, R. A. 1993, PhRvB, 48, 9973
Schmitt, B., De Bergh, C., & Festou, M. 1998, Solar System Ices (Dordrecht: Springer Science+Business Media)
Sears, F. W. 1952, An Introduction to Thermodynamics, The Kinetic Theory of Gases, and Statistical Mechanics (2nd ed.; London: Addison-Wesley)

Shi, J., Fama, M., Teolis, B. D., & Baragiola, R. A. 2010, NIMPB, 268, 2888
Showalter, M. R., Cuzzi, J. N., & Larson, S. M. 1991, Icar, 94, 451
Spencer, J. R., Pearl, J. C., Segura, M., et al. 2006, Sci, 311, 1401
Stevenson, K. P., Kimmel, G. A., Dohnalek, Z., Smith, R. S., & Kay, B. D. 1999, Sci, 283, 1505
Teolis, B. D., Perry, M. E., Magee, B. A., et al. 2010, JGR, 115, A09222
Tsekouras, A. A., Iedema, M. J., & Cowin, J. P. 1998, PhRvL, 80, 5798
Wahlund, J. E., Andre, M., Eriksson, A. I. E., et al. 2009, P&SS, 57, 1795
Wahlund, J. E., Bostrom, R., Gustafsson, G., et al. 2005, GeoRL, 32, L20S09
Waite, J. H., Jr., Combi, M. R., Ip, W.-H., et al. 2006, Sci, 311, 1419
Young, D. T., Berthelier, J. J., Blanc, M., et al. 2005, Sci, 307, 1262
Ziegler, J. F., & Biersack, J. P. 2013, Stopping and Range of Ions in Matter, SRIM.EXE, http://www.srim.org/SRIM/SRIMLEGL.htm